last melting in an ^{16}O-poor gas, probably in the chondrule-forming region.

The observed differences in grain size between the core and the mantle of TS26 (see Supplementary Fig. 2a) suggests that melting was incomplete and was followed by relatively fast cooling. The absence of Wark–Lovering rim layers around TS26 could also be due to the inferred melting episode. The high abundance of relict chondrule-like material in the outer portion of TS26 (see Supplementary Fig. 2b) suggests there was a high abundance of dust in the region where melting occurred, consistent with the dusty environment inferred for chondrule formation[2]. The low $(^{26}Al/^{27}Al)_0$ ratios observed in ABC and TS26 may have recorded their late-stage re-melting during incorporation of the chondrule fragments. We note, however, that because Allende experienced thermal metamorphism that may have disturbed the ^{26}Al-^{26}Mg systematics in CAIs and chondrules[25], the exact age difference between the formation of CAIs ABC and TS26 and their re-melting should be considered with caution.

The proposed multi-stage formation history of ABC and TS26 is consistent with the extended (~2 Myr) formation time of several other igneous CAI from CV chondrites inferred from a range of the $(^{26}Al/^{27}Al)_0$ ratios within a single inclusion and petrographic observations[26,27]. The late-stage melting and oxygen isotopic exchange of ABC and TS26 are also consistent with the recently proposed model for the global evolution of the oxygen isotope composition of the inner solar nebula gas from ^{16}O-rich to ^{16}O-poor with time[28,29]. The fact that many CAIs show no evidence for being affected by chondrule heating suggests that the chondrule-forming events were highly localized. □

Received 17 December 2004; accepted 11 February 2005; doi:10.1038/nature03470.

1. MacPherson, G. J. in *Treatise on Geochemistry* (eds Holland, H. D. & Turekian, K. K.) Vol. 1, *Meteorites, Comets and Planets* (ed. Davis, A. M.) 201–246 (Elsevier-Pergamon, Oxford, 2003).
2. Desch, S. J. & Connolly, H. C. A model of the thermal processing of particles in the solar nebula shocks: Application to the cooling rates of chondrules. *Meteorit. Planet. Sci.* **37,** 183–207 (2002).
3. Amelin, Y., Krot, A. N., Hutcheon, I. D. & Ulyanov, A. A. Lead isotopic ages of chondrules and calcium-aluminum-rich inclusions. *Science* **297,** 1678–1683 (2002).
4. Amelin, Y., Krot, A. N. & Twelker, E. Pb isotopic age of the CB chondrite Gujba, and the duration of the chondrule formation interval. *Geochim. Cosmochim. Acta* **68,** abstr. E958 (2004).
5. Itoh, S. & Yurimoto, H. Contemporaneous formation of chondrules and refractory inclusions in the early Solar System. *Nature* **423,** 728–731 (2003).
6. Krot, A. N. & Keil, K. Anorthite-rich chondrules in CR and CH carbonaceous chondrites: Genetic link between Ca, Al-rich inclusions and ferromagnesian chondrules. *Meteorit. Planet. Sci.* **37,** 91–111 (2002).
7. Krot, A. N., Hutcheon, I. D. & Keil, K. Anorthite-rich chondrules in the reduced CV chondrites: evidence for complex formation history and genetic links between CAIs and ferromagnesian chondrules. *Meteorit. Planet. Sci.* **37,** 155–182 (2002).
8. Krot, A. N. *et al.* Ca,Al-rich inclusions, amoeboid olivine aggregates, and Al-rich chondrules from the unique carbonaceous chondrite Acfer 094: I. Mineralogy and petrology. *Geochim. Cosmochim. Acta* **68,** 2167–2184 (2004).
9. Maruyama, S., Yurimoto, H. & Sueno, S. Oxygen isotope evidence regarding the formation of spinel-bearing chondrules. *Earth Planet. Sci. Lett.* **169,** 165–171 (1999).
10. Maruyama, S. & Yurimoto, H. Relationships among O, Mg isotopes and the petrography of two spinel-bearing chondrules. *Geochim. Cosmochim. Acta* **67,** 3943–3957 (2003).
11. McKeegan, K. D. & Davis, A. M. in *Treatise on Geochemistry* (eds Holland, H. D. & Turekian, K. K.) Vol. 1, *Meteorites, Comets and Planets* (ed. Davis, A. M.) 431–461 (Elsevier-Pergamon, Oxford, 2003).
12. Grossman, L., Ebel, D. S. & Simon, S. B. Formation of refractory inclusions by evaporation of condensate precursors. *Geochim. Cosmochim. Acta* **66,** 145–161 (2002).
13. Wark, D. A. & Lovering, J. F. Marker events in the early solar system: Evidence from rims on Ca-Al-rich inclusions in carbonaceous chondrites. *Proc. Lunar Planet. Sci. Conf.* **8,** 95–112 (1977).
14. Galy, A., Young, E. D., Ash, R. D. & O'Nions, R. K. The formation of chondrules at high gas pressures in the solar nebula. *Science* **290,** 1751–1753 (2000).
15. Alexander, C. M. O'D. & Wang, J. Iron isotopes in chondrules: Implications for the role of evaporation during chondrule formation. *Meteorit. Planet. Sci.* **36,** 419–428 (2001).
16. Scott, E. R. D. & Krot, A. N. in *Treatise on Geochemistry* (eds Holland, H. D. & Turekian, K. K.) Vol. 1, *Meteorites, Comets and Planets* (ed. Davis, A. M.) 143–200 (Elsevier-Pergamon, Oxford, 2003).
17. Bizzarro, M., Baker, J. A. & Haack, H. Mg isotope evidence for contemporaneous formation of chondrules and refractory inclusions. *Nature* **431,** 275–278 (2004).
18. MacDougall, J. D., Kerridge, J. F. & Phinney, D. Refractory ABC. *Lunar Planet. Sci.* **12,** 643–645 (1981).
19. Wark, D. A. Plagioclase-rich inclusions in carbonaceous chondrite meteorites: Liquid condensates? *Geochim. Cosmochim. Acta* **51,** 221–242 (1987).
20. Krot, A. N., McKeegan, K. D., Leshin, L. A., MacPherson, G. J. & Scott, E. R. D. Existence of an ^{16}O-rich gaseous reservoir in the solar nebula. *Science* **295,** 1051–1054 (2002).
21. Krot, A. N., Fagan, T. J., Yurimoto, H. & Petaev, M. I. Origin of low-Ca pyroxene in amoeboid olivine aggregates: Evidence from oxygen isotopic compositions. *Geochim. Cosmochim. Acta* (in the press).
22. McKeegan, K. D. & Leshin, L. A. in *Stable Isotope Geochemistry* (eds Valley, J. W. & Cole, D. R.) 279–378 (Reviews in Mineralogy & Geochemistry, Vol. 43, Mineralogical Society of America, Washington DC, 2001).
23. Yurimoto, H., Ito, M. & Nagasawa, H. Oxygen isotope exchange between refractory inclusion in Allende and solar nebula gas. *Science* **282,** 1874–1877 (1998).
24. Nagashima, K., Yoshitake, M. & Yurimoto, H. in *Workshop on "Chondrites and the Protoplanetary Disk"* 153–154 (University of Hawaii at Manoa, 2004); available at ⟨http://www.lpi.usra.edu/meetings/chondrites2004/pdf/9072.pdf⟩.
25. Yurimoto, H., Koike, O., Nagahara, H., Morioka, M. & Nagasawa, H. Heterogeneous distribution of Mg isotopes in anorthite single crystal from Type B CAIs in Allende meteorite. *Lunar Planet. Sci.* **31,** 1593 (2000).
26. MacPherson, G. J. & Davis, A. M. A petrologic and ion microprobe study of a Vigarano Type B refractory inclusion: Evolution by multiple stages of alteration and melting. *Geochim. Cosmochim. Acta* **57,** 231–243 (1989).
27. Hsu, W., Wasserburg, G. J. & Huss, G. R. High time resolution by use of the ^{26}Al chronometer in the multistage formation of a CAI. *Earth Planet. Sci. Lett.* **182,** 15–29 (2000).
28. Yurimoto, H. & Kuramoto, K. Molecular cloud origin for the oxygen isotope heterogeneity in the solar system. *Science* **305,** 1763–1766 (2004).
29. Krot, A. N. *et al.* Evolution of oxygen isotopic composition in the inner solar nebula *Astrophys. J.* (in the press).

Supplementary Information accompanies the paper on **www.nature.com/nature**.

Acknowledgements Financial support for this project was provided by NASA (A.N.K., I.D.H., G.J.M.) and Monkasho (H.Y.). We thank R. H. Hewins for comments and suggestions.

Competing interests statement The authors declare that they have no competing financial interests.

Correspondence and requests for materials should be addressed to A.N.K. (sasha@higp.hawaii.edu).

Controlled multiple quantum coherences of nuclear spins in a nanometre-scale device

Go Yusa[1], Koji Muraki[1], Kei Takashina[1], Katsushi Hashimoto[2]* & Yoshiro Hirayama[1,2]

[1]*NTT Basic Research Laboratories, NTT Corporation, 3-1 Morinosato-Wakamiya, Atsugi 243-0198, Japan*
[2]*SORST Program, Japan Science and Technology Agency (JST), 4-1-8 Honmachi, Kawaguchi, Saitama 331-0012, Japan*

* Present address: Institute of Applied Physics, Hamburg University, Jungiusstraβe 11, D-20355 Hamburg, Germany

The analytical technique of nuclear magnetic resonance (NMR[1,2]) is based on coherent quantum mechanical superposition of nuclear spin states. Recently, NMR has received considerable renewed interest in the context of quantum computation and information processing[3–11], which require controlled coherent qubit operations. However, standard NMR is not suitable for the implementation of realistic scalable devices, which would require all-electrical control and the means to detect microscopic quantities of coherent nuclear spins. Here we present a self-contained NMR semiconductor device that can control nuclear spins in a nanometre-scale region. Our approach enables the direct detection of (otherwise invisible) multiple quantum coherences between levels separated by more than one quantum of spin angular momentum. This microscopic high sensitivity NMR technique is especially suitable for probing materials whose nuclei contain multiple spin levels, and may form the basis of a versatile multiple qubit device.

Nuclei often possess total spin I greater than a half. Under static magnetic field B_0, therefore, $2I + 1$ states $|m\rangle$ equally spaced in energy by the Zeeman energy $\hbar\omega_0$ are formed according to the Zeeman effect (Fig. 1e). Here, $\hbar$ is the reduced Planck's constant such that ω_0 would be the resonant angular frequency of NMR between any pair of adjacent states. After appropriate polarization,

pulsed radio frequency (r.f.) electromagnetic field can be applied to achieve a coherent superposition $|\Psi\rangle = \sum_{m=+I}^{m=-I} a_m|m\rangle$ of nuclear spins with arbitrary complex amplitude a_m by controlling two out of three readily tunable parameters[1,12]; the time length τ_P of the r.f. pulse, the intensity B_1 of the magnetic component of the r.f. field and the offset $\hbar(\omega_R - \omega)$ between the energies of the r.f. field $\hbar\omega$ and the resonant transition $\hbar\omega_R$. Therefore, nuclei forming multiple spin levels have a large variety of possible coherent combinations. However, multiple quantum coherence is not directly detectable by conventional NMR as it does not produce transverse magnetization $\mathbf{M}_{x,y}$ (Fig. 1a), which conventional NMR detects. Our objective here is to produce a method that does not rely upon electromagnetic coupling of $\mathbf{M}_{x,y}$ to a pick-up coil[13–16], and to control and detect not only the single but also the multiple quantum coherences of nuclear spins in a nanoscale region by all-electrical means.

We fabricated a monolithic semiconductor device integrated with a point contact channel, which is a narrow constriction of a two-dimensional electron gas, and an antenna gate for locally irradiating the channel with an r.f. field (Fig. 1b). In this structure, we can selectively polarize nuclear spins in this nanometre-scale point contact region, while keeping those elsewhere in thermal equilibrium[17] (see Methods). With polarization followed by r.f. pulse irradiation, the resistance of the point contact falls, and then gradually increases again over a time period of the order of $\sim 10^2$–10^3 s and reaches the steady state value at polarization. We therefore interpret ΔR, the change in resistance directly before and after the pulse, to have a direct relationship with M_z, which is the longitudinal magnetization induced by the altered population of nuclear spin states. This in turn corresponds to the projection of the probability amplitude of the nuclear spin state $|\Psi\rangle$ onto the z axis (Fig. 1a).

The channel consists of ^{69}Ga, ^{71}Ga and ^{75}As, each having total spin $I = 3/2$. Thus, for each nuclide under B_0 (Fig. 1a), four equally spaced energy states $|m\rangle = |3/2\rangle, |1/2\rangle, |-1/2\rangle, |-3/2\rangle$ are formed (Fig. 1e, orange arrows). However, the nuclei experience the effects of an electric field gradient due to their host crystal, which shift the energy states through the electric quadrupolar interaction by energies $+\Delta$ and $-\Delta$ for $|\pm 3/2\rangle$ and $|\pm 1/2\rangle$, respectively[1,12,18,19]. The energy difference between adjacent states is, therefore, shifted by $\pm 2\Delta$ from $\hbar\omega_0$, allowing three possible resonances, at $\hbar\omega_0 - 2\Delta$, $\hbar\omega_0$ and $\hbar\omega_0 + 2\Delta$ (Fig. 1e, red arrows). According to energy and angular momentum conservation rules, several transitions are possible. For convenience of the later discussion, we label possible transitions by superscripts, for example, $^{75}As^{II}$ or $^{69}Ga^{IV/2}$, in which numerators, I, II,…, VI specify transitions and denominators 1, 2 and 3 represent the number of photons n, the second quantization of the r.f. field, involved in the transition.

Spectra of ΔR as a function of τ_P show three oscillations at low B_1 (Fig. 2a). These oscillations can be well fitted by damped oscillations[12] $\propto 1 - \cos(\Omega_R\tau_P)\exp(-\tau_P/T_2)$ with oscillation frequency Ω_R and decoherence time T_2, showing that ΔR is indeed linearly related to the projection of the probability amplitude of $|\Psi\rangle$ onto the z axis and to the longitudinal magnetization M_z. In a geometrical representation[1,12,20] of superpositional states of a two-level system (the Bloch sphere), the oscillations at $\hbar\omega_0$ (denoted by $^{75}As^{II}$ in Fig. 2d) correspond to the rotation of a state $|\Psi^{II}\rangle$ whose path describes a great circle passing through localized states $|1/2\rangle$ and $|-1/2\rangle$ periodically as the angle $\Omega_R\tau_P$ is swept. Therefore, the oscillations at $\hbar\omega_0$ represent a single quantum coherence between levels separated by a single quantum of angular momentum ($\Delta m = 1$). Similar oscillations seen in the lower- and higher-energy peaks of the spectra (denoted respectively by $^{75}As^{I}$ and $^{75}As^{III}$ in Fig. 2d) are also due to single quantum coherence, their energy shift being $\pm 2\Delta$ from $\hbar\omega_0$.

When B_1 is increased, two slow oscillations (denoted by $^{75}As^{IV/2,V/2}$ in Fig. 2e) are observed in the spectra (Fig. 2b) between the three single quantum oscillations. The peak energies of $^{75}As^{IV/2,V/2}$ are shifted from $\hbar\omega_0$ by $\pm\Delta$. When the peak energies of $^{75}As^{IV/2,V/2}$ are doubled ($= 2(\hbar\omega_0 \pm \Delta)$), the resulting values are exactly the energy separations between $|-3/2\rangle$ and $|1/2\rangle$ and between $|-1/2\rangle$ and $|3/2\rangle$ (Fig. 1e). These can be assigned to double quantum coherent oscillations between two levels separated by two quanta of angular momentum ($\Delta m = 2$) driven by two-photon transitions (IV/2 and V/2 in Fig. 1e). By increasing B_1 further, a new peak (denoted by $^{75}As^{VI/3}$ in Fig. 2f) appears at $\hbar\omega_0$ (Fig. 2c). The energy difference between $|-3/2\rangle$ and $|3/2\rangle$ is equal to $3\hbar\omega_0$ regardless of the quadrupolar interaction (Fig. 1e). Therefore, the narrow peak (VI/3) can be assigned to triple quantum coherence between $|-3/2\rangle$ and

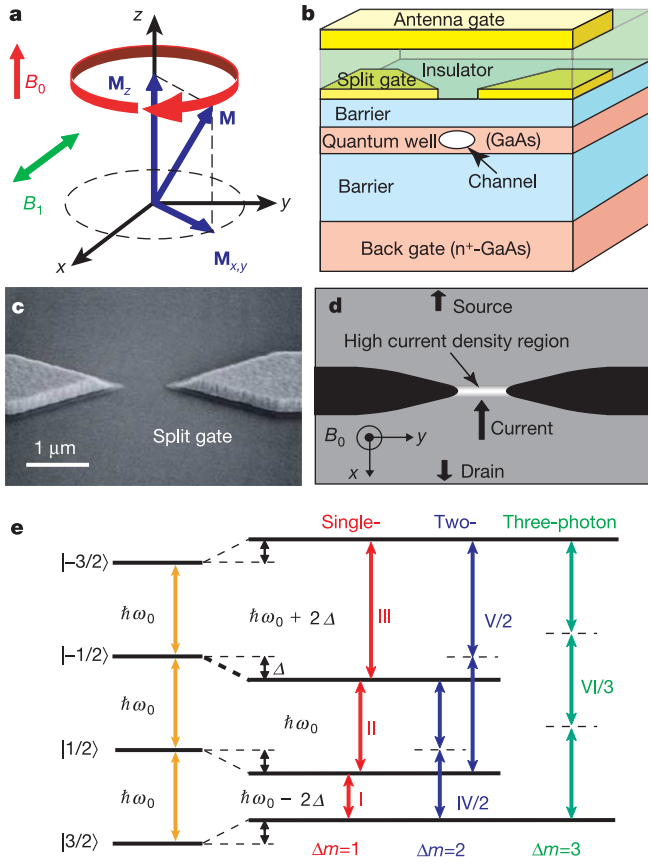

Figure 1 Schematic diagrams illustrating the main features of our device and the experimental system. **a**, Schematic illustration of the magnetization vector **M** of an ensemble of nuclear spins under a static magnetic field B_0 and an r.f. field. (B_1 is the magnetic field component of the r.f. field.) The transverse component $\mathbf{M}_{x,y}$ is precessing in the x–y plane (Larmor precession), while the longitudinal component M_z is static along B_0. **b**, Schematic illustration of a cross-sectional view of the device. The structure contains a 20-nm GaAs quantum well with AlGaAs barrier layers and an n^+-GaAs substrate that functions as a back-gate electrode to control electron density. A pair of Schottky split gates defines the point contact channel indicated by a white ellipse. The antenna gate is electrically isolated from the split gates by an insulator. **c**, Scanning electron microscope image of the split gates beneath the antenna gate. The gap between the gates is 600 nm, which is narrow enough to observe quantized conductance steps of $2e^2/h$ at $B_0 = 0$, where h is Planck's constant and e is the elementary charge. **d**, Schematic illustration of the plane view of the point contact channel. By applying negative voltage to the split gate, the depletion regions (shown in black) are formed. By passing current (~7 nA) between the source and drain at Landau level filling factor $\nu = 2/3$ (refs 26–28), nuclear spins are polarized in the point contact region, where the current density is locally high. The resistance across the point contact is measured by a four-terminal method in constant-current mode to achieve a steady state of nuclear spin polarization[17]. **e**, Schematic energy level diagram of nuclear spin states for $I = 3/2$ with (right) and without (left) electric quadrupolar interactions. See main text for nomenclature details.

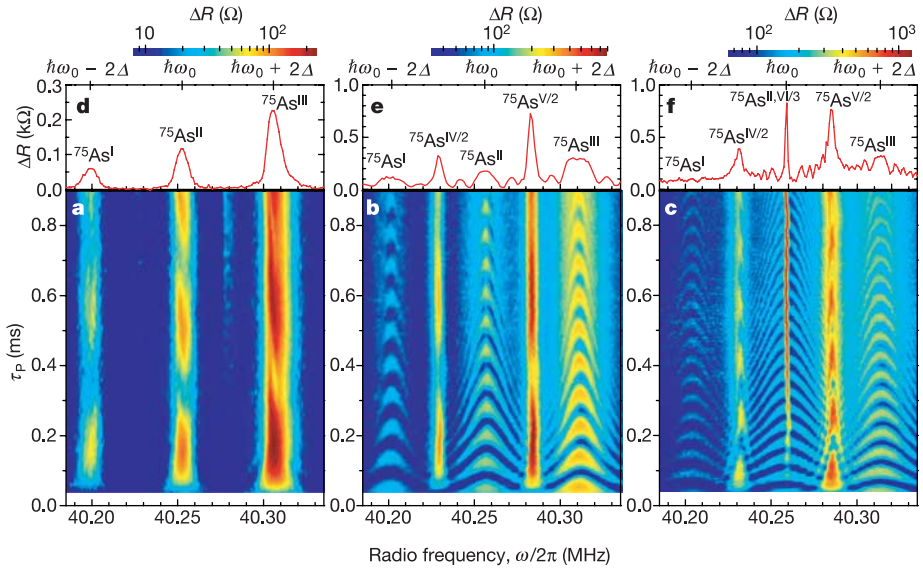

Figure 2 Spectra of ΔR for ^{75}As at three different intensities B_1, which is proportional to the square root of the output power $P_{\mathrm{r.f.}}$ from an r.f. generator. The measurement was performed at $B_0 = 5.5$ T at 0.1 K. ΔR is colour coded on a logarithmic scale for clarity. (The resolution is not equal for the three panels.) **a**, Colour plot of ΔR as a function of τ_P at $P_{\mathrm{r.f.}} = 0$ dBm. **b**, 13 dBm. **c**, 20 dBm. **d**, Spectrum at $\tau_P = 0.12$ ms taken from **a**. **e**, Spectrum at $\tau_P = 0.126$ ms taken from **b**. **f**, Spectrum at $\tau_P = 0.426$ ms taken from **c**.

$|3/2\rangle$, involving three photons with energy $\hbar\omega_0$. Single and triple quantum coherences are produced and detected by a single r.f. pulse.

All six coherences are observed for all three nuclides (^{75}As, ^{69}Ga and ^{71}Ga). Whereas the observation of clear oscillations due to the three-photon transition is hampered by r.f. power limitations for $^{75}As^{VI/3}$, such a high power regime is readily accessible for ^{69}Ga, which has a larger gyromagnetic ratio[1,12,18,19]. ΔR of ^{69}Ga as a function of τ_P at $\hbar\omega_0$ reveals slow oscillations of $^{69}Ga^{VI/3}$ superimposed on the fast oscillations of $^{69}Ga^{II}$ (Fig. 3a). These two oscillations clearly show different dependence on B_1 in their oscillation frequencies Ω_R (Fig. 3b). At low B_1, only the fast oscillations of $^{69}Ga^{II}$ are visible (line A in Fig. 3a). With increasing B_1, the slow oscillations of $^{69}Ga^{VI/3}$ start to appear (line B), and its frequency rapidly increases in a manner expected for a multi-photon process[21,22].

As coherent oscillations are observed at any resonant energy $\hbar\omega_R$, coherent superpositions $|\Psi\rangle$ of any two states, which lie on the great circle of the Bloch sphere, are achieved. As $\hbar\omega$ shifts away from $\hbar\omega_R$, the oscillation frequency Ω increases while the oscillation amplitude decreases, resulting in off-resonance tails (Fig. 2). This behaviour corresponds to the trajectory of $|\Psi\rangle$ for constant $\hbar\omega$, moving from the great circle on the Bloch sphere, shrinking towards convergence

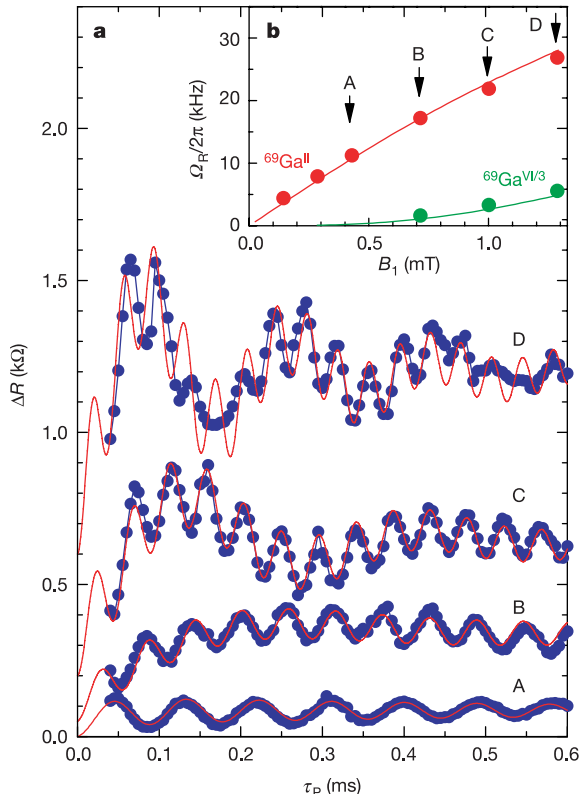

Figure 3 Behaviour of ΔR for ^{69}Ga at $\omega_0/2\pi$. **a**, ΔR at $\omega_0/2\pi = 64.7141$ MHz for ^{69}Ga as a function of τ_P at several different values of B_1. Line A: $P_{\mathrm{r.f.}} = 9.54$ dBm, B: 14 dBm, C: 17 dBm, D: 19 dBm. The measurement was performed at $B_0 = 6.3$ T at 75 mK. The data have been offset for clarity. Red lines are phenomenologically fitted by two oscillatory components with two different Ω_Rs and T_2s by $/\mathrm{i}] > \propto 1 - \cos(\Omega_R \tau_P) \exp(-\tau_P/T_2)$. The T_2 of the fast oscillations of $^{69}Ga^{II}$ is between ~0.5 and 1.5 ms, while that of $^{69}Ga^{VI/3}$ is ~0.2 ms. In line D, at the first and third minima of the slow oscillations of $^{69}Ga^{VI/3}$, the amplitude of $^{69}Ga^{II}$ is clearly smaller and the oscillation frequency of $^{69}Ga^{II}$ is faster than the fit. Also, similar discrepancy from the simple superpositional oscillations is observed at $\hbar\omega_0$ for ^{75}As. **b**, Oscillation frequency $\Omega_R/2\pi$ as a function of B_1 for $^{69}Ga^{II,VI/3}$. Lines show the theoretical behaviour obtained by taking Fourier transforms of the numerical calculations determined in the main text. The quadrupolar frequency (15.2 kHz) and the gyromagnetic ratio (1.17×10^7 s^{-1} T^{-1}) used in the calculation are estimated from the experiment.

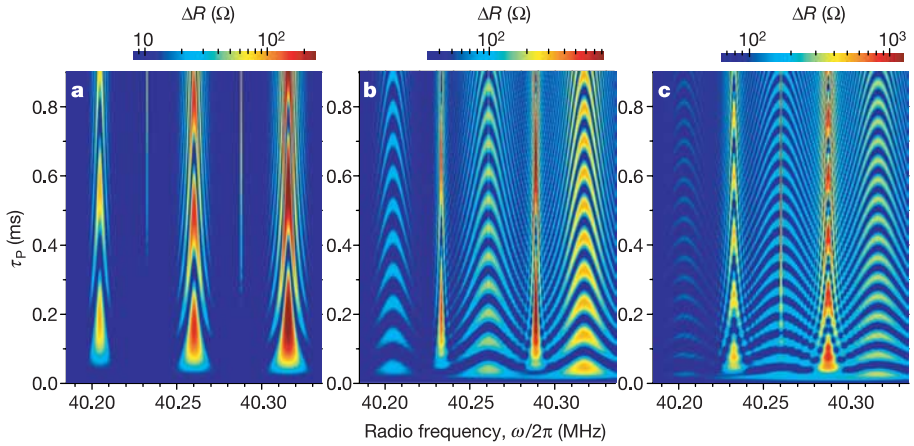

Figure 4 Colour plots showing calculated values of ΔR. The exact quantum mechanical evolution of ^{75}As is numerically simulated using the rotating frame approximation[1,10,12,23]. The nuclear spin hamiltonian used here is $H = H_Z + H_0 + \gamma\hbar B_1 \cos(\omega t) I_x$. Here $H_Z = -\gamma\hbar B_0 I_z$ is the Zeeman term, where γ is the gyromagnetic ratio of each nuclide; $H_Q = \Delta/3[3I_z^2 - I(I+1)]$ is the quadrupolar term, and $\gamma\hbar B_1 \cos(\omega t) I_x$ is the magnetic field term of the r.f. H is transformed into H_{rot} in the rotating frame, and used to calculate the expectation value of M_z (refs 10, 23). Relaxation processes are not taken into account. $\Delta/h = 26.9$ kHz and $\gamma = 7.32 \times 10^6\ s^{-1}\ T^{-1}$ are estimated from Fig. 2. The initial population ρ_0 and the conversion coefficient between the change in the resistance and the calculated evolution of M_z are determined by fitting the spectrum in Fig. 2c at $\tau_P = 82\ \mu s$, which is short compared with $T_2 \approx 1$ ms. **a**, $P_{r.f.} = 0$ dBm ($B_1 = 0.2$ mT); **b**, 13 dBm (0.85 mT); **c**, 20 dBm (1.4 mT).

at one localized state $|m\rangle$. This demonstrates that coherent superpositions of any two states with any order Δm of quantum coherence can be achieved with any arbitrary complex amplitude by a single r.f. pulse at constant B_1, controlled by τ_P and offset energy $\hbar(\omega_R - \omega)$. (See Methods.)

We have simulated the quantum mechanical evolution and thereby the expectation value of the longitudinal magnetization M_z of an ensemble of spin $I = 3/2$ systems using the rotating-frame approximation[1,10,12,23] (Fig. 4). The calculation, in which the only input parameter is the r.f. power B_1, can reproduce the overall features of the data (Fig. 2) remarkably well, including not only the frequencies of all observed oscillations but also the behaviour of off-resonance tails. Their widths for higher Δm are scaled down by the photon number n and are therefore narrower. The oscillation amplitudes for higher Δm are larger than those for $\Delta m = 1$, reflecting greater change in the angular momentum Δm. The calculated B_1 dependence of the oscillation frequency agrees well with the data (Fig. 3b). These excellent agreements, both qualitative and quantitative, justify our interpretation in terms of multi-photon processes. Furthermore, fitting the relative oscillation amplitudes of different transitions allows us to determine the initial polarization before an r.f. pulse $\rho_0 = \{\rho_{|3/2\rangle}, \rho_{|1/2\rangle}, \rho_{|-1/2\rangle}, \rho_{|-3/2\rangle}\}$ to be {0, 0.1, 0.28, 0.62}, which is surprisingly far from equilibrium (an apparent spin temperature of -3 mK). Moreover, the fact that a single conversion coefficient of 898 Ω per nuclear magneton can not only fit all data for different B_1 but also for different Δm clearly shows the linear relationship between M_z and ΔR, thus confirming our detection mechanism.

At resonant frequencies with only one coherence visible, the temporal decay of the oscillations can be fitted well by introducing a phenomenological decoherence time T_2. At $\hbar\omega_0$, where the single and triple coherences coincide, the data can be fitted by assuming two independent T_2s for two coherences when the r.f. power is not too high (lines A, B and C in Fig. 3a). At the highest power, however, deviation from such a simple model becomes discernible (line D). We confirm that numerical calculation, which incorporates the interference between different coherences within the same nucleus, cannot reconcile this deviation. This in turn leads us to speculate that additional effects, such as coupling between different nuclei, start to play a role.

As we have demonstrated, three single, two double and one triple quantum coherences for one nuclide, 18 in total for three nuclides, are completely controlled by all-electrical means. One of the simplest applications of our device would be for quantum search engines[9,10,23,24] using the Grover algorithm[25], which can be performed using multi-level nuclear spins. Our device is not in itself a scalable multi-qubit system, but if different coherences could be entangled—for example, by controlling coupled coherence between different nuclei as suggested above—it would allow quantum entanglement[20] of nuclear spins to express superpositions of different binary strings. The device is also likely to find application as a quantum-information storage device for quantum mechanical states of electrons[11], as its decoherence time is orders of magnitude longer than any other likely candidate. Using conduction electrons as a mediator, such devices could be integrated into solid-state quantum circuits incorporating multilevel nuclear spin systems. □

Methods

Mechanisms for polarization and detection

Under special conditions of electron density and B_0 in the fractional quantum Hall regime[26–28], two states with different electron spin polarizations become nearly degenerate in energy. When sufficiently large current is applied in such cases, nuclear spins in contact with the two-dimensional electron system are polarized as a result of flip-flop scattering through the contact hyperfine interaction. The hyperfine field produced by the polarized nuclei modifies the Zeeman energy of electrons and hence the back scattering probability, as manifested by a change in the resistance[27]. In our device, this occurs only when a certain negative voltage ($\lesssim -0.3$ V) is applied to the split gates, and a current above a threshold is passed. Owing to the narrow constriction (Fig. 1b–d), the local current density exceeds the threshold only in the point contact region, thereby locally producing nuclear polarization far from equilibrium. For detecting the nuclear polarization after the manipulation with the r.f. pulse, the same condition (in terms of the electron density, B_0 and the split-gate voltage) is used, as it also ensures high sensitivity of the resistance to the nuclear spin polarization. If we estimate the dimensions of the nanoscale point contact region (Fig. 1b) to be $\sim 200 \times 200\ nm^2$ (area) and ~ 10 nm (thickness), the number of nuclei in the resulting volume is of the order of $\sim 10^8$ or less, several orders of magnitude smaller than the detection limit of conventional NMR (10^{11}–10^{13}).

Towards coherence over all four levels

In this Letter we mainly discuss multiple coherences between two spin states out of four with a single r.f. frequency. Controlling coherence over all four levels requires an r.f. pulse with three different energies, which could be readily achieved using three r.f. generators and a conventional r.f. combiner.

Received 5 November 2004; accepted 14 February 2005; doi:10.1038/nature03456.

1. Ernst, R. R., Bodenhausen, G. & Wokaun, A. *Principles of Nuclear Magnetic Resonance in One and Two Dimensions* (Oxford Univ. Press, Oxford, 1987).
2. Liang, Z. P. & Lauterbur, P. C. *Principles of Magnetic Resonance Imaging: A Signal Processing Perspective* (IEEE Press, Piscataway, 1999).

3. DiVincenzo, D. P. Quantum computation. *Science* **270,** 255–261 (1995).
4. Chuang, I. L., Vandersypen, L. M. K., Zhou, X., Leung, D. W. & Lloyd, S. Experimental realization of a quantum algorithm. *Nature* **393,** 143–146 (1998).
5. Kane, B. E. A silicon-based nuclear spin quantum computer. *Nature* **393,** 133–137 (1998).
6. Nakamura, Y., Pashkin, Yu. A. & Tsai, J. S. Coherent control of macroscopic quantum states in a single-Cooper-pair box. *Nature* **398,** 786–788 (1999).
7. Mooij, J. E. *et al.* Josephson persistent-current qubit. *Science* **285,** 1036–1039 (1999).
8. Vandersypen, L. M. K. *et al.* Experimental realization of Shor's quantum factoring algorithm using nuclear magnetic resonance. *Nature* **414,** 883–887 (2001).
9. Leuenberger, M. N. & Loss, D. Quantum computing in molecular magnets. *Nature* **410,** 789–793 (2001).
10. Leuenberger, M. N., Loss, D., Poggio, M. & Awschalom, D. D. Quantum information processing with large nuclear spins in GaAs semiconductors. *Phys. Rev. Lett.* **89,** 207601 (2002).
11. Taylor, J. M., Marcus, C. M. & Lukin, M. D. Long-lived memory for mesoscopic quantum bits. *Phys. Rev. Lett.* **90,** 206803 (2003).
12. Levitt, M. H. *Spin Dynamics* (Wiley, New York, 2002).
13. Wald, K. R., Kouwenhoven, L. P., McEuen, P. L., van der Vaart, N. C. & Foxon, C. T. Local dynamic nuclear polarization using quantum point contacts. *Phys. Rev. Lett.* **73,** 1011–1014 (1994).
14. Gammon, D. *et al.* Nuclear spectroscopy in single quantum dots: nanoscopic Raman scattering and nuclear magnetic resonance. *Science* **277,** 85–88 (1997).
15. Kikkwawa, J. M. & Awschalom, D. D. All-optical magnetic resonance in semiconductors. *Science* **287,** 473–476 (2000).
16. Machida, T., Yamazaki, T., Ikushima, K. & Komiyama, S. Coherent control of nuclear-spin system in a quantum Hall device. *Appl. Phys. Lett.* **82,** 409–411 (2003).
17. Yusa, G., Hashimoto, K., Muraki, K., Saku, T. & Hirayama, Y. Self-sustaining resistance oscillations: Electron-nuclear spin coupling in mesoscopic quantum Hall devices. *Phys. Rev. B* **69,** 161–302 (2004).
18. Salis, G., Awschalom, D. D., Ohno, Y. & Ohno, H. Origin of enhanced dynamic nuclear polarization and all-optical nuclear magnetic resonance in GaAs quantum wells. *Phys. Rev. B* **64,** 195304 (2001).
19. Eickhoff, M., Lenzman, B., Flinn, G. & Suter, D. Coupling mechanisms for optically induced NMR in GaAs quantum wells. *Phys. Rev. B* **65,** 125301 (2002).
20. Nielsen, M. A. & Chuang, I. L. *Quantum Computation and Quantum Information* (Cambridge Univ. Press, Cambridge, 2003).
21. Cohen-Tannoudji, C., Dupont-Roc, J. & Grynberg, G. *Atom-photon Interactions: Basic Processes and Applications* 488–489 (Wiley, New York, 1998).
22. Wokaun, A. & Ernst, R. R. Selective excitation and detection in multilevel spin systems: Application of single transition operators. *J. Chem. Phys.* **67,** 1752–1758 (1977).
23. Leuenberger, M. N. & Loss, D. Grover algorithm for large nuclear spins in semiconductors. *Phys. Rev. B* **68,** 165317 (2003).
24. Ahn, J., Weinacht, T. C. & Bucksbaum, P. H. Information storage and retrieval through quantum phase. *Science* **287,** 463–465 (2000).
25. Grover, L. K. Quantum computers can search arbitrarily large databases by a single query. *Phys. Rev. Lett.* **79,** 4709–4712 (1997).
26. Kronmüller, S. *et al.* New resistance maxima in the fractional quantum Hall effect regime. *Phys. Rev. Lett.* **81,** 2526–2529 (1998).
27. Hashimoto, K., Muraki, K., Saku, T. & Hirayama, Y. Electrically controlled nuclear spin polarization and relaxation by quantum-Hall states. *Phys. Rev. Lett.* **88,** 176601 (2002).
28. Smet, J. H. *et al.* Gate-voltage control of spin interactions between electrons and nuclei in a semiconductor. *Nature* **415,** 281–286 (2002).

Acknowledgements The authors are grateful to T. Fujisawa, Y. Tokura, S. Sasaki, K. Semba, S. Saito, K. Ono, S. Tarucha, T. Machida, T. Ota and N. Kumada for discussions.

Competing interests statement The authors declare that they have no competing financial interests.

Correspondence and requests for materials should be addressed to G.Y. (yusa@NTTBRL.jp) or K.M. (muraki@will.brl.ntt.co.jp).

Seasonal prediction of hurricane activity reaching the coast of the United States

Mark A. Saunders & Adam S. Lea

Benfield Hazard Research Centre, Department of Space and Climate Physics, University College London, Holmbury St Mary, Dorking, Surrey RH5 6NT, UK

Much of the property damage from natural hazards in the United States is caused by landfalling hurricanes[1–3]—strong tropical cyclones that reach the coast. For the southeastern Atlantic coast of the US, a statistical method for forecasting the occurrence of landfalling hurricanes for the season ahead has been reported[4], but the physical mechanisms linking the predictor variables to the frequency of hurricanes remain unclear. Here we present a statistical model that uses July wind anomalies between 1950 and 2003 to predict with significant and useful skill the wind energy of US landfalling hurricanes for the following main hurricane season (August to October). We have identified six regions over North America and over the east Pacific and North Atlantic oceans where July wind anomalies, averaged between heights of 925 and 400 mbar, exhibit a stationary and significant link to the energy of landfalling hurricanes during the subsequent hurricane season. The wind anomalies in these regions are indicative of atmospheric circulation patterns that either favour or hinder evolving hurricanes from reaching US shores.

The North Atlantic hurricane season extends from 1 June to 30 November. However, 86% of US hurricane strikes and 96% of US intense (major) hurricane strikes in 1950–2003 occurred after 1 August[5]. The large year-to-year variability in the number of hurricanes making US landfall (range zero to six since 1950) means that skilful seasonal forecasts of activity would benefit a spectrum of decision makers by reducing risk and uncertainty. Seasonal hurricane forecasting was pioneered[6] in the mid-1980s for the North Atlantic. Assessments of seasonal forecast skill for US landfalling hurricane activity have been made for the southeast US from 1 August[4] and for the whole US in September[7]. Work has also examined the probability of US hurricane landfall and damage as a function of the sign and strength of the El Niño/Southern Oscillation (ENSO)[8–11]. However, with one exception[4], none of these studies has claimed skill that is significant, robust and high enough to be practically useful. For example, the hindcast correlation skill for predicting the number of US landfalling hurricanes in September 1950–2000 is only ~0.38 (ref. 7).

Seasonal US landfalling hurricane activity is referenced usually in terms of the numbers of tropical storms, hurricanes or intense hurricanes making US landfall. We introduce the National Oceanic and Atmospheric Administration's Accumulated Cyclone Energy (ACE) index[12] as a single more appropriate measure for categorizing 'seasonal US landfalling hurricane activity'. We call this the US ACE index, and define it as the sum of the squares of hourly maximum sustained wind speeds (in units of knots) from all tropical cyclones over the US mainland (including those that have changed to extra-tropical) that have winds of at least tropical storm strength. This value is then reduced by a factor of 6 for compatibility with the ACE index at sea, which is computed from wind values every 6 h (ref. 12). The US ACE index is effectively a wind energy index indicating the cumulative wind energy from all US-striking tropical storms, hurricanes and intense hurricanes occurring during a given season. We compute the US ACE index using the maximum sustained wind speed data from the US National Hurricane Center's North Atlantic hurricane database[13].

Our analysis also uses monthly wind data averaged between 925 and 400 mbar (about 750 to 7,000 m above sea level) from the National Center for Environmental Prediction/National Center for Atmospheric Research reanalysis[14] during 1950–2003. The motion of hurricanes is determined by height-averaged winds between these levels[15,16]. US hurricane total (economic) and insured loss data are obtained from ref. 3 (updated economic losses through to the end of 2003 are provided by C. W. Landsea) and from ref. 17 (insured losses for 2000–03 are provided by the US Property Claims Service) respectively for the period 1950–2003. All correlation coefficients (r_{rank}) refer to the Spearman rank correlation coefficient. All statistical significances are two-sided values corrected for serial autocorrelation[18,19].

The US ACE index 1950–2003 is linked significantly to tropospheric height-averaged wind anomalies occurring over North America, the east Pacific and the North Atlantic both before (July) and during the main Atlantic hurricane season. August, September and October are the main months for landfalling hurricane wind energy, with 82% of the annual US ACE index occurring therein. Figure 1 displays for July (Fig. 1a) and